

# Highly Efficient Picture-Based Prediction of PM<sub>2.5</sub> Concentration

Ke Gu , Junfei Qiao, *Member, IEEE*, and Xiaoli Li

**Abstract**—Air pollutants do much harm to human safety. In particular, the fine particulate matter (PM<sub>2.5</sub>), a complex air pollutant which is composed of the particles beneath the aerodynamic diameters of 2.5  $\mu\text{m}$ , very possibly causes severe diseases since it is easy to intrude into the lungs. To that end, in this paper, we design a new picture-based predictor of PM<sub>2.5</sub> concentration (PPPC), which employs the pictures acquired using mobile phones or cameras to make a real-time estimation of PM<sub>2.5</sub> concentration. First, using a large body of pictures which were captured under the good weather conditions, i.e., very low PM<sub>2.5</sub> concentration, naturalness statistics (NS) models are built upon entropy features in spatial and transform domains. Second, for a novel picture, we measure its deviation degree from the above-mentioned NS models, considering the fact that the naturalness of a picture tends to reduce with the PM<sub>2.5</sub> concentration increased. Third, a simple nonlinear function is introduced to map the deviation degree to the PM<sub>2.5</sub> concentration. In comparison to existing relevant state-of-the-art predictors, sufficient experimental results manifest the superiority of the proposed PPPC model in terms of prediction accuracy and implementation efficiency.

**Index Terms**—Naturalness statistics (NS), nonlinear mapping, particulate matter (PM<sub>2.5</sub>) concentration, pictures, predictor.

## I. INTRODUCTION

QUALITY diagnosis and stabilisation analysis have long served as important and practical research topics for the modern industry, which constantly receive massive attention [1]–[3]. The past few decades have witnessed a frustrating environmental phenomenon that the rapid urbanization and industrialization are causing and accelerating the deterioration of air quality, and this has become an alarming global crisis.

Manuscript received December 21, 2017; revised March 24, 2018; accepted May 3, 2018. Date of publication June 1, 2018; date of current version November 30, 2018. This work was supported in part by the National Science Foundation of China under Grant 61473034, Grant 61673053, and Grant 61703009, in part by the Young Elite Scientist Sponsorship Program by China Association for Science and Technology under Grant 2017QNRC001, in part by the Young Top-Notch Talents Team Program of Beijing Excellent Talents Funding under Grant 2017000026833ZK40 and in part by the Beijing Nova Programme Interdisciplinary Cooperation Project under Grant Z161100004916041. (*Corresponding author: Ke Gu.*)

The authors are with the Beijing Key Laboratory of Computational Intelligence and Intelligent System, Faculty of Information Technology, Beijing University of Technology, Beijing 100124, China (e-mail: guke.doctor@gmail.com; junfeiq@bjut.edu.cn; lixiaolibjut@bjut.edu.cn).

Color versions of one or more of the figures in this paper are available online at <http://ieeexplore.ieee.org>.

Digital Object Identifier 10.1109/TIE.2018.2840515

Among all the typical air pollutants, the fine particulate matter (PM<sub>2.5</sub>) with the aerodynamic diameters of 2.5  $\mu\text{m}$  or less has aroused an increased number of attention because those fine particles are able to easily transmit hazardous chemicals into the human bodies, and thus bring about serious diseases by damaging cerebrovascular, cardiovascular, and respiratory functions. Current measurements or instruments for monitoring PM<sub>2.5</sub> concentration primarily rely on gauging its weight with physicochemical methods, such as Gravimetric method,  $\beta$ -ray absorption method, micro oscillating balance method, etc., [4]. By contrast, the  $\beta$ -ray absorption method is popular due to its wide application scopes. In implementation, PM<sub>2.5</sub> is first gathered on a filter paper followed by a bunch of  $\beta$  rays is irradiated. When the rays go through the filter paper and particulate matter, it attenuates because of scattering. The attenuation degree is proportional to the weight of PM<sub>2.5</sub>. Therefore, the weight of PM<sub>2.5</sub> can be counted based on the attenuation of  $\beta$  rays. However, the above-mentioned sensor-based PM<sub>2.5</sub> measurements inevitably introduce high cost of setup and maintenance, and this must make them unavailable to the majority of regions. So, one kind of effective, efficient, and handy solution is the pursuit of replacing the traditional sensor-based PM<sub>2.5</sub> measurements.

To date, due to the mighty functions and broad application areas, smart phones have become one of the most significant tools in daily lives, accompanying us at anywhere and anytime. In certain degrees, smart phones have even turned out to be a real human sixth sense. By means of mobile phones, we are able to easily take photos at any time, to describe and record the things happening around us followed by being sent and saved through ubiquitous wireless networks into private or public clouds for personal access or shared to the others. It will provide such an affordable way to monitor air quality if the PM<sub>2.5</sub> concentration can be efficiently and effectively estimated from the captured pictures. In spite of great values, very few works have been devoted to this type of research so far. To the best of our knowledge, only Liu *et al.* put forward a solution, which learns six features extracted from pictures [5]. The dark channel prior was first used to estimate the image transmission, and then contrast and entropy of pictures were measured as features. Besides, the influences of the color of sky and the location of sun on the estimation of PM<sub>2.5</sub> concentration were taken into consideration as well and used for features. The authors deploy the support vector regressor [6] to combine all the features to predict the PM<sub>2.5</sub> concentration. Nonetheless, the model highly depends on manually marked reference regions with different depths beforehand, and this largely limits its application scopes.

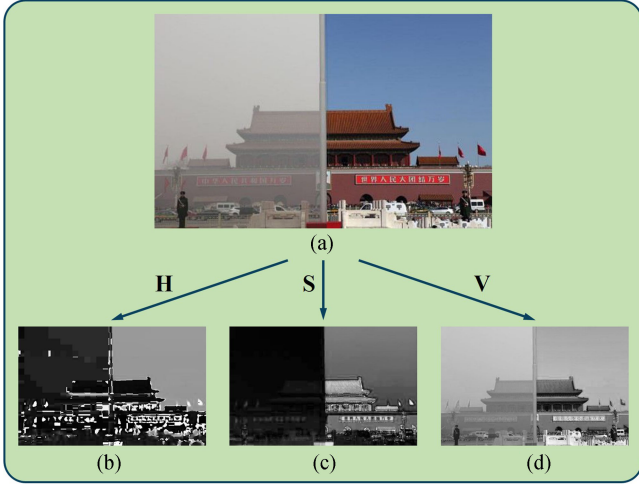


**Fig. 1.** Comparison of hue, saturation and value channels in photos captured under bad and good weather. (a) Mixed sample picture. (b) Hue map. (c) Saturation map. (d) Value map.

This paper designs a completely blind predictor of PM2.5 concentration, without any manual assistance, such as human-labeled areas of interest. Early works have shown that camera-captured natural images are of multiple statistical regularities [7]–[11], and these have been successfully utilized for image restoration, quality measurement, and so forth. Essentially, a straightforward reflection of PM2.5 variations is to alter the contrast of pictures, particularly in terms of image saturation. For illustration consider the example in Fig. 1. We present a mixed image of “Tian An Men,” the left and right halves of which are two photos captured under the bad and good weather, respectively, and the corresponding hue, saturation, and value maps [12]. As can be seen, the photo taken under the bad weather tends to be higher order, while the photo acquired under the good weather tends to be lower order. The theoretical foundation behind this observation is twofold: 1) the increase of PM2.5 reduces the visibility and moreover the contrast of captured photos [13]–[15]; and 2) the saturation of each pixel in a picture tends to be zero and the whole saturation map tends toward stable and orderly, because the saturation can be deemed as the similarity between one color and its closest natural spectrum color [16], which will drop to a very small level when the PM2.5 concentration is large.

According to the observation and explanation stated above, we carry out a tentative analysis to the orders of saturation map in spatial and transform domains. Entropy is a landmark measure of the order and thereby employed in this research. Via substantial experiments, it was observed that the entropy features of photos acquired under the good weather (i.e., very low PM2.5 concentration) exhibit the transparent naturalness statistics (NS), the extreme-value distribution for the spatial domain, and the Gaussian distribution for the transform domain, respectively. Simultaneously, it was also found that the above NS models will be broken as the weather becomes worse or equivalently the PM2.5 concentration increases. In practical applications, given a new photo, we first extract the entropy features in spatial and transform domains. Then, we measure the likelihood of naturalness between the entropy features and NS models, which were estab-

lished based on a great number of pictures captured under the good weather. Notice that the aforementioned measure is not the absolute prediction of PM2.5 concentration, but just used to tell the relative value. Thus, a nonlinear mapping is eventually exerted on the likelihood of naturalness toward the reliable PM2.5 estimation. Results of thorough experiments confirm the superiority of the proposed predictor, with the prediction accuracy higher than 80%, as compared with many relevant competitors.

In this paper, there are two major contributions, which are summarized as follows.

- 1) To the best of our knowledge, we are the first to use the pictures for estimating the PM2.5 concentration, without any additional auxiliary information such as depth.
- 2) This research constructs the first NS model applicable to the PM2.5 estimation using a large class of photos that were taken under the condition of very low PM2.5 concentration.

The remainder of this paper is outlined as follows. Section II illustrates the implementation details about the proposed picture-based predictor of PM2.5 concentration (PPPC). In Section III, we conduct the performance measure and comparison between the PPPC predictor and state-of-the-art relevant prediction models. Some concluding remarks and future works are provided in Section IV.

## II. METHODOLOGY

In this section, we will detailedly illustrate the proposed picture-based PPPC prediction model from the three aspects as follows: feature extraction, likelihood measure, and nonlinear mapping.

### A. Feature Extraction

The direct reflection of a rise in PM2.5 concentration is to make one picture toward: colorless and low information amount. Extracting the saturation map from a photo is a good solution to the above-mentioned first factor (i.e., colorless), since we can consider saturation to be the similarity between one color and its closest natural spectrum color [16]. As given in Fig. 1, as the PM2.5 concentration elevates, the saturation map quickly reduces to a very small value. In this condition, each pixel’s saturation in a picture tends to become zero and the overall saturation map tends to be stable and orderly. Therefore, given an RGB-format picture, we first extract its saturation map after transforming it into the HSV color space from the RGB space

$$S(x, y) = \begin{cases} \frac{U(x, y) - V(x, y)}{U(x, y)}, & \text{if } U(x, y) \neq 0 \\ 0, & \text{otherwise} \end{cases} \quad (1)$$

where  $x$  and  $y$  are separately the pixel index in horizontal and vertical directions;  $U(x, y) = \max[R(x, y), G(x, y), B(x, y)]$ ;  $V(x, y) = \min[R(x, y), G(x, y), B(x, y)]$ .

Entropy is the most commonly used measure of the order, so we then compute it in the spatial domain of the saturation map [20]

$$H_S = - \sum_{i=1}^H \sum_{j=1}^W P[S(i, j)] \cdot \log P[S(i, j)] \quad (2)$$

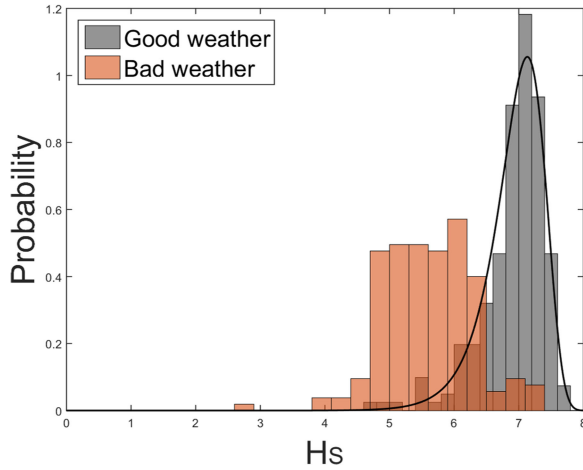


Fig. 2. Histograms of the entropy value  $H_S$  in the spatial domain of the saturation map. Photos acquired under the good weather are well-fitted by the extreme-value probability density function.

where  $H$  and  $W$  independently indicate the height and width of saturation map;  $P[S(i, j)]$  denotes the probability distribution of  $S(i, j)$ . We gathered greater than 5000 pictures captured under the good weather, i.e., PM2.5 concentration less than  $12 \mu\text{g}/\text{m}^3$ . The advanced partial least square (APLS) [17], which merges the improved PLS (IPLS) [18] and the modified partial robust M-regression algorithm [19], is applied to remove the outliers. We make use of (1) and (2) to compute the spatial entropy of these images and plot the histogram, as illustrated in Fig. 2. The histogram evidently provides an NS regularity: it fits the extreme-value distribution well. For comparison, we further collected about 200 pictures that were acquired under the bad weather, namely PM2.5 concentration superior to  $200 \mu\text{g}/\text{m}^3$ . Similarly, we plot them in Fig. 2 as well. One can obviously see that the  $H_S$  value decreases as the PM2.5 concentration increases. Hence, the entropy value  $H_S$  in the spatial domain of the saturation map is considered as the first feature.

The transform domain is a frequently applied and effective solution to many scientific research and practical application problems, e.g., video coding [21]–[23], industrial electronics [24]–[27], image restoration [28]–[30], etc. This paper takes advantage of the Haar wavelet decomposition, because its mother wavelet is concise

$$\psi(t) = \begin{cases} 1 & 0 \leq t \leq 0.5 \\ -1 & 0.5 \leq t \leq 1 \\ 0 & \text{otherwise} \end{cases} \quad (3)$$

and the associated scaling function  $\phi(t)$  is simple

$$\phi(t) = \begin{cases} 1 & 0 \leq t \leq 2 \\ 0 & \text{otherwise} \end{cases} \quad (4)$$

In this paper, the Haar wavelet shows good performance and more powerful wavelet bases, such as db3, bior2.4 and sym2, as well as the decompositions based on Curvelet, Contourlet, Bandelet, etc., will be taken into consideration in the future work. A scale-space orientation decomposition is applied to the wavelet domain feature extraction. In implementation, we deploy the

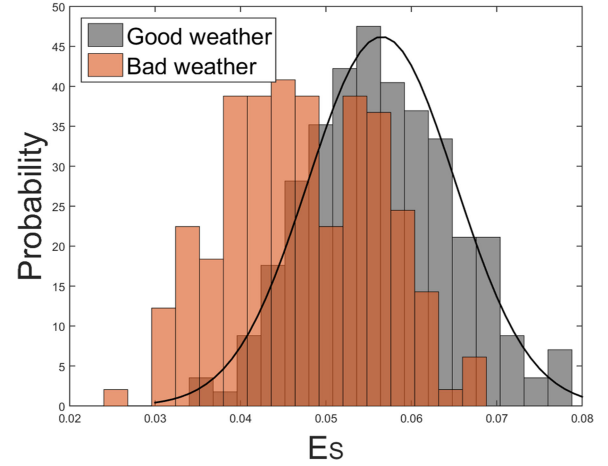


Fig. 3. Histograms of the entropy value  $E_S$  in the transform domain of the saturation map. Photos acquired under the good weather are nicely fitted by the Gaussian probability density function.

multiscale steerable pyramid structure along the vertical, horizontal, and diagonal directions (LH, HL, and HH). The crucial detailed information is saved in high-frequency subbands for conveying the semantic information through the multiscale representation. The saturation map is decomposed into five scales. Considering that the LH and HL subbands in each scale are of similar statistics, we combine these two subbands together, and thus generate a total of ten subbands. Then, we compute the entropy of the wavelet coefficients in each subband

$$E_Z^k = - \sum_{i=1}^{H_Z^k} \sum_{j=1}^{W_Z^k} P[Z_k(i, j)] \cdot \log P[Z_k(i, j)] \quad (5)$$

where  $Z = \{\text{LH} + \text{HL}, \text{HH}\}$ ,  $H_Z^k$  and  $W_Z^k$  are the height and width of the  $Z$  subband at the  $k$ th scale;  $P[Z_k(i, j)]$  denotes the probability distribution of coefficients in the  $Z$  subband at the  $k$ th scale. We emphasize the impact of the HH subbands, and thereby, define the overall entropy to be

$$E_S = \frac{1}{K} \sum_{k=1}^K \frac{E_{\text{LH}+\text{HL}}^k + \psi \cdot E_{\text{HH}}^k}{1 + \psi} \quad (6)$$

where  $K$  is the total number of scales, and  $\psi$  is a weighting parameter higher than one. Here, we assign  $K = 5$  and  $\psi = 4$ . We also compute the  $E_S$  value of the 5000 photos captured under the good weather and display the histogram in Fig. 3. As seen, the histogram nicely fits the Gaussian distribution. Likewise, we employ the 200 pictures acquired under the bad weather for comparison and observe that they are deviated from the Gaussian distribution mentioned above, as provided in Fig. 3. Therefore, the entropy value  $E_S$  in the transform domain of the saturation map is used as the second feature.

## B. Likelihood Measure

In the context, we have found two good features. For the pictures captured under the good weather, the two features of these images well-conform to the certain NS regularities. By contrast, the injection of PM2.5 destroys the NS regularities,

clearly deviated from the extreme-value distribution and the Gaussian distribution, as exhibited in Figs. 2 and 3. Given a new photo, its associated PM2.5 concentration can be reflected by its likelihood of naturalness based on the aforementioned NS models. To compute the likelihood, the NS models (including the model parameters) should be determined beforehand.

First of all, for the entropy feature of the saturation map in the spatial domain, as shown in Fig. 2, its histogram can be nicely fitted by an extreme value probability density function which is expressed by

$$Q_V = \frac{1}{d} \exp \left[ \frac{H_S - u}{d} - \exp \left( \frac{H_S - u}{d} \right) \right] \quad (7)$$

where  $Q_V$  represents the likelihood of a picture being natural given its spatial entropy value  $H_S$ ,  $u$  and  $d$  are, respectively, the model parameters to be fitted. In this paper, we exploit the maximum likelihood estimation (MLE) [31] to search for the optimal model parameters by maximizing the probability of observations generated by the model

$$\arg \max_{\xi} Q_V(\mathbf{f}; \xi) \quad (8)$$

where  $\xi = \{u, d\}$ ,  $\mathbf{f} = \{f_1, f_2, \dots, f_n\}$ , and  $n$  is the number of all the observations. We suppose that each observation is independent of all others and apply the natural logarithm to (8), yielding

$$\begin{aligned} L(\mathbf{f}; \xi) &= \arg \max_{\xi} Q_V(\mathbf{f}; \xi) \\ &= \arg \max_{\xi} \sum_{i=1}^n \ln Q_V(f_i; \xi) \\ &= \arg \max_{\xi} \sum_{i=1}^n \frac{f_i - u}{d} - \sum_{i=1}^n \exp \left( \frac{f_i - u}{d} \right) - n \ln d. \end{aligned} \quad (9)$$

We obtain the partial derivative of the function  $L(\mathbf{f}; \xi)$  with respect to  $u$  and  $d$

$$\frac{\partial L}{\partial u} = \frac{n}{d} - \frac{1}{d} \sum_{i=1}^n \exp \left( \frac{u - f_i}{d} \right) \quad (10)$$

$$\frac{\partial L}{\partial d} = nd - \sum_{i=1}^n (f_i - u) + \sum_{i=1}^n (f_i - u) \exp \left( \frac{f_i - u}{d} \right). \quad (11)$$

Letting the two equations above equal to zero, we derive the optimal estimations of model parameters

$$\frac{n}{d} - \frac{1}{d} \sum_{i=1}^n \exp \left( \frac{u - f_i}{d} \right) = 0 \quad (12)$$

$$nd - \sum_{i=1}^n (f_i - u) + \sum_{i=1}^n (f_i - u) \exp \left( \frac{u - f_i}{d} \right) = 0. \quad (13)$$

Obviously, we cannot directly find the analytical solution of the aforesaid two equations. This paper employs the Newton–Raphson to iteratively find the numerical solution and finally

obtains the optimal estimations:  $u = 7.1325$  and  $d = 0.3485$ . In Fig. 2, we plot the fitting curve based on these model parameters.

Next, as for the entropy feature of the saturation map in the transform domain, as shown in Fig. 3, the histogram can be well-fitted by a Gaussian probability density function as defined as follows:

$$Q_G = \frac{1}{\sqrt{2\pi}\sigma} \exp \left[ -\frac{(E_S - \mu)^2}{2\sigma^2} \right] \quad (14)$$

where  $Q_G$  means the likelihood of naturalness given a photo with its transform-based entropy value  $E_S$  and  $\mu$  and  $\sigma$  separately indicate the model parameters to be fitted. Similarly, we use the MLE to solve the best estimations of model parameters and derive  $\mu = 0.0565$  and  $\sigma = 0.0086$ . In Fig. 3, we deploy these model parameters to plot the fitting curve.

Given a new photo, we first extract its saturation map and the corresponding spatial and transform-based entropy features ( $H_S$  and  $E_S$ ) using (2)–(6). Next, we calculate the likelihood  $Q_V$  and  $Q_G$  based on (7)–(14). The overall likelihood of naturalness is ultimately defined as the multiplication of two components as follows:

$$Q = Q_V^w \cdot Q_G^{1-w} \quad (15)$$

where  $w$  is a weighting coefficient. In this paper, we simply assign  $w = 0.5$  to make the two components have the same contribution.

### C. Nonlinear Mapping

The overall likelihood  $Q$  is not the absolute prediction of PM2.5 concentration, but used to provide the relative value. In other words, for a group of pictures, the larger the overall likelihood, the smaller the PM2.5 concentration. Therefore, a nonlinear mapping is needed to convert the overall likelihood of naturalness to the final PM2.5 estimation.

According to the above concern, we require a nonlinear mapping which improves the performance accuracy but does not influence the monotonicity of input data. There are three logistic functions in line with this demand as follows:

$$S_E(Q) = \frac{\alpha_1}{1 + \exp \left( \frac{\alpha_2 - Q}{\alpha_3} \right)} \quad (16)$$

$$S_E(Q) = \frac{\beta_1 - \beta_2}{1 + \exp \left( \frac{\beta_3 - Q}{\beta_4} \right)} + \beta_2 \quad (17)$$

$$S_E(Q) = \gamma_1 \left[ \frac{1}{2} - \frac{1}{1 + \exp \left( \frac{Q - \gamma_2}{\gamma_3} \right)} \right] + \gamma_4 Q + \gamma_5 \quad (18)$$

where  $\{\alpha_1, \dots, \alpha_3\}$ ,  $\{\beta_1, \dots, \beta_4\}$ , and  $\{\gamma_1, \dots, \gamma_5\}$  are three teams of free parameters to be ascertained during the curve fitting process. Via comparison to be illustrated in Section III, there exist very few differences between the above three functions, and consequently, in this paper, we select the simplest three-parameter nonlinear function.

In implementation, given a novel picture with its overall likelihood  $Q$ , we make use of (16) to generate the estimated score  $S_E$ , namely the final estimation of PM2.5 concentration. Toward enhancing the readability of this paper, as shown in Fig. 4,

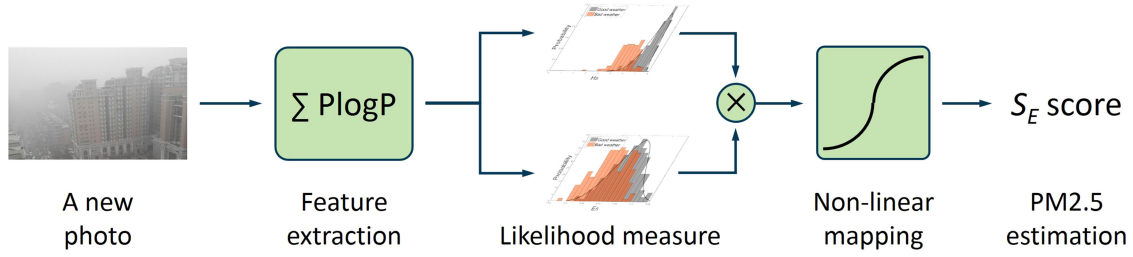


Fig. 4. Basic flowchart to illustrate how to use the PPC predictor to estimate PM2.5 concentration.

we present a basic flowchart to illustrate the whole process of the proposed PPC model.

### III. EXPERIMENTS

This section is devoted to demonstrating the superiority of the proposed method in terms of prediction performance and implementation speed. To this aim, this section is composed of the subsequent eight aspects: testing dataset, competing methods, performance benchmarking, numerical comparison, visualized comparison, statistical significance comparison, runtime comparison, and discussion.

#### A. Testing Dataset

We first established a specific picture dataset for PM2.5 concentration estimation, which involves 750 pictures in total. Those pictures contain different scenes, such as square, fly-over, temple, roads, lakes, buildings, cars, parks, etc. They were captured at the diversified locations and seasons and under the various weather situations during the last three years. All photos are of a wide range of image resolutions from  $500 \times 261$  to  $978 \times 550$ . As for each of pictures above, we retrieved the associated PM2.5 value from the historical data of hourly PM2.5 concentration measurements provided by the U.S. embassy in Beijing. The PM2.5 concentration has a range from 1 to 423, and we plot their histogram as exhibited in Fig. 5.

#### B. Competing Methods

In this paper, we have collected ten state-of-the-art or popular relevant prediction models, which can be divided into three types according to their application scenarios. The first type is composed of three lately devised models based on NS, namely IL-NIQE [32], ASIQE [33], and LPSI [34]. In this paper, the authors have established some NS models using high-quality pictures and their quality scores will decrease when several variations are exerted on the pictures. The second type involves a pair of state-of-the-art models, namely NIQMC [35] and BIQME [36]. The two studies were developed specific to the quality evaluation of contrast-altered pictures, relevant to the picture-based prediction of PM2.5 concentration since PM2.5 has an immense impact on the camera-captured pictures. The third type consists of five popular algorithms devoted to sharpness/blurriness measurements, namely S3 [37], FISH [38], FISHbb [38], ARISM [39], and BIBLE [40].

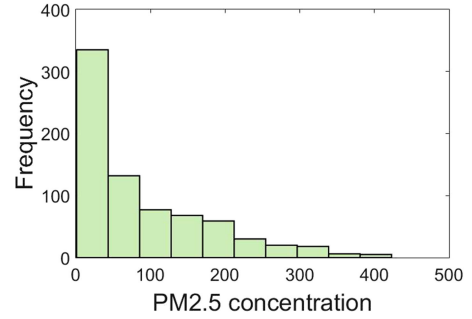


Fig. 5. Histogram of PM2.5 concentrations of 750 pictures.

#### C. Performance Benchmarking

This paper introduces three evaluation measures in light of their different functions. The first measure is the linear correlation coefficient (LCC), which gauges the prediction accuracy between a couple of vectors. The LCC is calculated by

$$\text{LCC} = \frac{\sum_{m=1}^M \tilde{a}_m \cdot \tilde{b}_m}{\sqrt{\sum_{m=1}^M \tilde{a}_m^2 \cdot \sum_{m=1}^M \tilde{b}_m^2}} \times 100\% \quad (19)$$

where  $\tilde{a} = a_m - \hat{a}$  and  $\tilde{b} = b_m - \hat{b}$  with  $\hat{a} = \sum_{m=1}^M a_m$  and  $\hat{b} = \sum_{m=1}^M b_m$  (the average values of vectors) and  $M$  is the number of the elements in the vector. The second one is the Kendall's rank-order correlation coefficient (KRC) used for estimating the strength of dependence of the two vectors. The KRC is expressed by

$$\text{KRC} = \frac{2(M_c - M_d)}{M^2 - M} \times 100\% \quad (20)$$

where  $M_c$  and  $M_d$  separately mean the numbers of concordant and discordant pairs in the dataset. And the last criterion is the root-mean-square error (RMSE), which concentrates on the prediction consistency, as defined as follows:

$$\text{RMSE} = \sqrt{\frac{1}{M} \sum_{m=1}^M (a_m - b_m)^2}. \quad (21)$$

Among the three evaluation criteria above, a good prediction model is wished to attain the high values in LCC and KRC, and simultaneously, the small value in RMSE.

**TABLE I**  
NUMERICAL PERFORMANCE COMPARISON BETWEEN THE TEN  
STATE-OF-THE-ART MODELS AND THE PROPOSED PPPC PREDICTOR

Models	TYPE	LCC	KRC	RMSE	RANK
IL-NIQE [32]	I	32.37%	17.26%	83.12	6
ASIQE [33]	I	12.13%	9.996%	87.21	9
LPSI [34]	I	4.070%	1.192%	87.78	10
NIQMC [35]	II	41.56%	29.60%	79.92	5
<b>BIQME [36]</b>	<b>II</b>	<b>54.28%</b>	<b>37.19%</b>	<b>73.78</b>	<b>2</b>
S3 [37]	III	30.60%	18.00%	83.65	7
<b>FISH [38]</b>	<b>III</b>	<b>46.23%</b>	<b>27.23%</b>	<b>77.91</b>	<b>3</b>
FISHbb [38]	III	42.85%	23.66%	79.39	4
ARISMC [39]	III	22.62%	13.30%	85.63	8
BIBLE [40]	III	2.613%	2.304%	87.83	11
<b>PPPC</b>	<b>IV</b>	<b>80.80%</b>	<b>60.79%</b>	<b>51.88</b>	<b>1</b>

#### D. Numerical Comparison

Based on the testing dataset and evaluation criteria stated above, we measure the correlation performance of each prediction model tested and implement the numerical comparison among them, as given in Table I. For convenient comparison, we have labeled the type of each competing model and offered the rank in view of their LCC scores. Notice that the type IV is associated to the proposed PPPC predictor. Evidently, in accordance to the LCC, KRC, and RMSE values, the PPPC model has achieved the optimal prediction performance, much better than other competitors. Specifically, the proposed PPPC model is the unique model whose LCC and KRC values are independently beyond 80% and 60%. As compared to the second-place BIQME method (highlighted in Table I), the PPPC predictor has acquired the relative performance gains of 49% in LCC and 63% in KRC, respectively. Further, the relative performance gains between the proposed model and the third-performing FISH algorithm is separately 75% in LCC and 123% in KRC.

In addition, let us see the rank of all the 11 competing models as given in Table I. We can find that, among the three types of prediction models, the entire two models in the second type (i.e., devoted to the contrast change), and part of models in the third type (i.e., specific to sharpness/blurriness assessment) have attained fair performance, whereas the performance of the first type of models based on NS is quite poor. More concretely, the reason why the proposed PPPC model outperforms the BIQME is that the BIQME deploys the features concerning NS as well as improper training instances which stem from man-made artificial contrast-changed images. By contrast with the BIBLE, the BIBLE only takes the features regarding image sharpness into account, but overlooks other influences, such as image color, contrast, etc. Inspired by these results, the features extracted based on contrast alteration and sharpness measure can be incorporated into the proposed PPPC method toward greater prediction performance in the future work.

It is noted that there are three alternative logistic functions for nonlinear mapping, and the three-parameter function is eventually used in the PPPC model. In this paper, we further compute and compare the correlation performance of them. The LCC, KRC, and RMSE values are as follows.

- 1) 80.80%, 60.79%, and 51.88 for the three-parameter function;
- 2) 81.07%, 60.79%, and 51.44 for the four-parameter function;
- 3) 81.09%, 60.79%, and 51.41 for the five-parameter function.

It is worth stressing that the KRC value of each nonlinear function is the same on account of the fact that those three functions do not change the monotonicity of input data. We are able to readily observe that, notwithstanding distinct values in LCC and RMSE, the differences among the three functions above are badly small and can be ignored to a large extent. As a consequence, we employ the simplest three-parameter logistic function in the proposed PPPC prediction model, since the decrease of free parameters has more potential for good generalization ability in most cases.

#### E. Visualized Comparison.

Scatter plots have offered a kind of straightforward comparison, and thus, we show the scatter plots of the PM2.5 estimations yielded by using the prediction model and the true PM2.5 concentrations measured based on the associated instruments. Considering that the majority of prediction models tested are of poor performance, this paper only deploys the top four models, namely NIQMC, BIQME, FISH, and the proposed PPPC, for visualized comparison, as shown in Fig. 6. In each scatter plot, we use the black dash lines to label the benchmark ideal prediction. It is quite clear that the proposed PPPC model has presented the impressive convergency and monotonicity, conspicuously exceeding the other three competitors.

#### F. Statistical Significance Comparison.

Apart from numerical and visualized comparisons, we also carry out the statistical significance comparison, because it can seek the differences between two prediction models which are not caused by some occasional factors but the prediction ability of a model itself. In this paper, we leverage the commonly used statistical f-test that follows a variance-based hypothesis and illustrates additional information regarding the relative performance of different prediction models. The hypothesis behind the f-test lies in that the residual differences of estimated and observed values of PM2.5 concentration follow a Gaussian distribution. The f-test examines whether a sample set has the equivalent distribution to the other and accordingly makes a statistically sound judgment about superiority or inferiority. In practice, we employ the f-test to compare the variances of two teams of prediction residuals: one team of prediction residuals from the differences between the PPPC's PM2.5 estimations and the true observed PM2.5 concentrations; and the other team between another testing model's PM2.5 estimations and the true values. Experimental results validate that the proposed PPPC

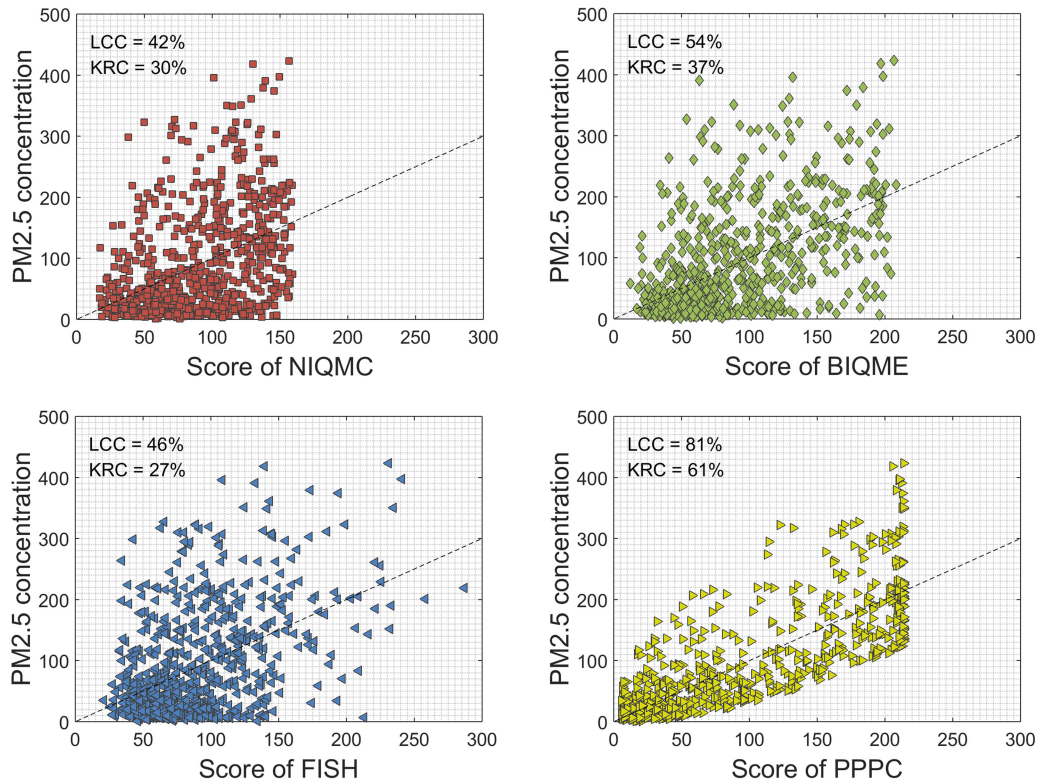


Fig. 6. Scatter plots of the PM<sub>2.5</sub> estimations derived by NIQMC, BIQME, FISH, and the PPC models and the true PM<sub>2.5</sub> concentrations measured using instruments on the testing dataset. The black dash lines are associated to the benchmark perfect prediction.

TABLE II  
RUNTIME COMPARISON OF 11 PREDICTION MODELS ON THE TESTING DATASET

Models	IL-NIQE [32]	ASIQE [33]	LPSI [34]	NIQMC [35]	BIQME [36]	S3 [37]	FISH [38]	FISHbb [38]	ARISMC [39]	BIBLE [40]	PPPC Proposed
Time (s)	4.4359	0.4507	<b>0.0177</b>	2.5529	0.9619	13.131	<b>0.0192</b>	0.5617	9.1973	1.6518	<b>0.0496</b>

model has delivered statistically greater performance than all of the other prediction models tested in this paper.

### G. Runtime Comparison

Ultimately, this paper computes and compares the runtime of 11 competing models (10 popular or state-of-the-art models and the proposed PPC model) using the overall 750 pictures in the testing dataset, because a well-designed model is expected to be of small runtime and high computational efficiency. This test is carried out by utilizing MATLAB2014a on a desktop computer with 64-bit operating system, 32 GB internal memory, and 3.4 GHz CPU processor. We tabulate the results in Table II and highlight the optimal three predictors for easy comparison. As seen, the proposed model works very efficiently, only consuming less than 0.05 s for calculating a picture, or equivalently, computing 20 pictures in 1 s. It deserves to emphasize that, in the aforesaid test, the proposed PPC method operates with a series computing. Therefore, the parallel computing might be introduced to remarkably reduce the runtime, because the spatial

entropy feature and transform-based entropy features in each of the five scales can be calculated independently.

### H. Discussion

Some multivariate statistical analysis methods, such as APLS [17] and IPLS [18], have been considered in building predictive models, and thus in one future work, they will be used for incorporating the features extracted based on the analysis of pictures better. Second, another work to be explored in the future will focus on the multimodal analysis through integrating the recurrent air quality predictor [41] with the proposed picture-backed PPC model. Finally, some crucial modifications, such as introducing other transform domains, advanced wavelet bases, or the measurements of image contrast and sharpness, will be tried to improve the PPC predictor.

## IV. CONCLUSION

In this paper, we focused on and addressed a crucial and practical problem—picture-based PM<sub>2.5</sub> concentration

prediction. Via observations and analyses, it was found that the orderly of picture saturation can nicely reflect the PM2.5 concentration. On this basis, this paper first extracted entropy features in the spatial and transform domains. Furthermore, applying a large number of pictures captured under the good weather, we established NS models of the above-mentioned two entropy features. By measuring the likelihood of naturalness between the entropy features and the statistics models, we are able to derive a relative value that reflects the possibility that a given picture has a small PM2.5 concentration. Finally, a simple nonlinear logistic function was used to map the measurement of likelihood to the estimation of PM2.5 concentration. Results of experiments validate that the proposed PPPC model has acquired the best correlation performance among all the models considered in terms of numerical and statistical significance comparisons. Moreover, the model also has the advantage of low computational cost. The picture dataset of PM2.5 and the implementation code of the PPPC model will be released at <https://kegu.netlify.com/>.

## REFERENCES

- [1] X. Xie, S. Yin, H. Gao, and O. Kaynak, "Asymptotic stability and stabilisation of uncertain delta operator systems with time-varying delays," *IET Control Theory Appl.*, vol. 7, no. 8, pp. 1071–1078, May 2013.
- [2] S. Yin, X. Xie, J. Lam, K. C. Cheung, and H. Gao, "An improved incremental learning approach for KPI prognosis of dynamic fuel cell system," *IEEE Trans. Cybern.*, vol. 46, no. 12, pp. 3135–3144, Dec. 2016.
- [3] S. Yin, X. Xie, and W. Sun, "A nonlinear process monitoring approach with locally weighted learning of available data," *IEEE Trans. Ind. Electron.*, vol. 64, no. 2, pp. 1507–1516, Feb. 2017.
- [4] J. C. Chow, "Measurement methods to determine compliance with ambient air quality standards for suspended particles," *J. Air Waste Manage. Assoc.*, vol. 45, no. 5, pp. 320–382, 1995.
- [5] C. Liu, F. Tsow, Y. Zou, and N. Tao, "Particle pollution estimation based on image analysis," *PLoS one*, vol. 11, no. 2, 2011, Art. no. e0145955.
- [6] C-C. Chang and C-J. Lin, "LIBSVM: a library for support vector machines," *ACM Trans. Intel. Syst. Technol.*, vol. 2, no. 3, Apr. 2011.
- [7] K. I. Kim and Y. Kwon, "Single image super-resolution using sparse registration and natural image prior," *IEEE Trans. Pattern Anal. Mach. Intell.*, vol. 32, no. 6, pp. 1127–1133, Jun. 2010.
- [8] J. Sun, J. Sun, Z. Xu, and H.-Y. Shum, "Gradient profile prior and its applications in image super-resolution and enhancement," *IEEE Trans. Image Process.*, vol. 20, no. 6, pp. 1529–1542, Jun. 2011.
- [9] A. Mittal, R. Soundararajan, and A. C. Bovik, "Making a 'completely blind' image quality analyzer," *IEEE Signal Process. Lett.*, pp. 209–212, vol. 22, no. 3, Mar. 2013.
- [10] K. Gu, V. Jakhetiya, J.-F. Qiao, X. Li, W. Lin, and D. Thalmann, "Model-based referenceless quality metric of 3D synthesized images using local image description," *IEEE Trans. Image Process.*, pp. 394–405, vol. 27, no. 1, Jan. 2018.
- [11] G. Yue, C. Hou, K. Gu, S. Mao, and W. Zhang, "Biologically inspired blind quality assessment of tone-mapped images," *IEEE Trans. Ind. Electron.*, pp. 2525–2536, vol. 65, no. 3, Mar. 2018.
- [12] 2018. [Online]. Available: [https://en.wikipedia.org/wiki/HSL\\_and\\_HSV](https://en.wikipedia.org/wiki/HSL_and_HSV)
- [13] D. E. Abbey, B. E. Ostro, G. Fraser, T. Vancuren, and R. J. Burchette, "Estimating fine particulates less than 2.5 microns in aerodynamic diameter (PM2.5) from airport visibility data in California," *J. Exposure Anal. Environ. Epidemiol.*, vol. 5, no. 2, pp. 161–180, Apr. 1995.
- [14] B. L. Davis and J. Guo, "Airborne particulate study in five cities of China," *Atmos. Environ.*, vol. 34, no. 17, pp. 2703–2711, Jan. 2000.
- [15] J.-L. Wang *et al.*, "Quantitative relationship between visibility and mass concentration of PM2.5 in Beijing," *J. Environ. Sci.*, vol. 18, no. 3, pp. 475–481, Jun. 2006.
- [16] M. D. Fairchild, *Color Appearance Models*. New York, NY, USA: Wiley, 2013.
- [17] X. Xie, W. Sun, and K. C. Cheung, "An advanced PLS approach for key performance indicator-related prediction and diagnosis in case of outliers," *IEEE Trans. Ind. Electron.*, vol. 63, no. 4, pp. 2587–2594, Apr. 2016.
- [18] S. Yin, X. Zhu, and O. Kaynak, "Improved PLS focused on key-performance-indicator-related fault diagnosis," *IEEE Trans. Ind. Electron.*, vol. 62, no. 3, pp. 1651–1658, Mar. 2015.
- [19] S. Serneels, C. Croux, P. Filzmoser, and P. J. Van Espen, "Partial robust M-regression," *Chemom. Intell. Lab.*, vol. 79, no. 1, pp. 55–64, Oct. 2005.
- [20] C. E. Shannon, "A mathematical theory of communication," *Bell Syst. Tech. J.*, vol. 27, pp. 379–423, Oct. 1948.
- [21] C. Christopoulos, A. Skodras, and T. Ebrahimi, "The JPEG2000 still image coding system: An overview," *Trans. Cons. Electron.*, vol. 46, no. 4, pp. 1103–1127, Nov. 2000.
- [22] H. Schwarz, D. Marpe, and T. Wiegand, "Overview of the scalable video coding extension of the H. 264/AVC standard," *IEEE Trans. Circuits Syst. Video Technol.*, vol. 17, no. 9, pp. 1103–1120, Sep. 2007.
- [23] G. J. Sullivan, J. Ohm, W.-J. Han, and T. Wiegand, "Overview of the high efficiency video coding (HEVC) standard," *IEEE Trans. Circuits Syst. Video Technol.*, vol. 22, no. 12, pp. 1649–1668, Dec. 2012.
- [24] R. Kumar, B. Singh, D. T. Shahani, and C. Jain, "Dual-tree complex wavelet transform-based control algorithm for power quality improvement in a distribution system," *IEEE Trans. Ind. Electron.*, vol. 64, no. 1, pp. 764–772, Jan. 2017.
- [25] H. Deng, Y. Zhang, and X.-G. Duan, "Wavelet transformation-based fuzzy reflex control for prosthetic hands to prevent slip," *IEEE Trans. Ind. Electron.*, vol. 64, no. 5, pp. 3718–3726, May 2017.
- [26] V. N. S. R. Jakka, A. Shukla, and G. D. Demetriades, "Dual-transformer-based asymmetrical triple-port active bridge (DT-ATAB) isolated DC-DC converter," *IEEE Trans. Ind. Electron.*, vol. 64, no. 6, pp. 4549–4560, Jun. 2017.
- [27] M. K. Metwaly, N. I. Elkalashy, and M. S. Zaky, "Discrete sine and cosine transforms for signal processing spectral overlap saliencies of induction machine," *IEEE Trans. Ind. Electron.*, vol. 65, no. 1, pp. 189–199, Jan. 2018.
- [28] R. Fattal, D. Lischinski, and M. Werman, "Gradient domain high dynamic range compression," *ACM Trans. Graph.*, vol. 27, no. 3, pp. 1–10, Jul. 2002.
- [29] M. Elad and M. Aharon, "Image denoising via sparse and redundant representations over learned dictionaries," *IEEE Trans. Image Process.*, vol. 15, no. 12, pp. 3736–3745, Dec. 2006.
- [30] K. Dabov, A. Foi, V. Katkovnik, and K. Egiazarian, "Image denoising by sparse 3-D transform-domain collaborative filtering," *IEEE Trans. Image Process.*, vol. 16, no. 8, pp. 2080–2095, Aug. 2007.
- [31] F. W. Scholz, "Maximum likelihood estimation," in *Encyclopedia of Statistical Sciences*, New York, NY, USA: Wiley, 1985.
- [32] L. Zhang, L. Zhang, and A. C. Bovik, "A feature-enriched completely blind image quality evaluator," *IEEE Trans. Image Process.*, vol. 24, no. 8, pp. 2579–2591, Aug. 2015.
- [33] K. Gu, J. Zhou, J.-F. Qiao, G. Zhai, W. Lin, and A. C. Bovik, "No-reference quality assessment of screen content pictures," *IEEE Trans. Image Process.*, vol. 26, no. 8, pp. 4005–4018, Aug. 2017.
- [34] Q. Wu, Z. Wang, and H. Li, "A highly efficient method for blind image quality assessment," in *Proc. IEEE Int. Conf. Image Process.*, Sep. 2015, pp. 339–343.
- [35] K. Gu, W. Lin, G. Zhai, X. Yang, W. Zhang, and C. W. Chen, "No-reference quality metric of contrast-distorted images based on information maximization," *IEEE Trans. Cybern.*, vol. 47, no. 12, pp. 4559–4565, Dec. 2017.
- [36] K. Gu, D. Tao, J.-F. Qiao, and W. Lin, "Learning a no-reference quality assessment model of enhanced images with big data," *IEEE Trans. Neural Netw. Learn. Syst.*, vol. 29, no. 4, pp. 1301–1313, Apr. 2018.
- [37] C. Vu, T. Phan, and D. Chandler, "S<sub>3</sub>: A spectral and spatial measure of local perceived sharpness in natural images," *IEEE Trans. Image Process.*, vol. 21, no. 3, pp. 934–945, Mar. 2012.
- [38] P. V. Vu and D. M. Chandler, "A fast wavelet-based algorithm for global and local image sharpness estimation," *IEEE Signal Process. Lett.*, vol. 19, no. 7, pp. 423–426, Jul. 2012.
- [39] K. Gu, G. Zhai, W. Lin, X. Yang, and W. Zhang, "No-reference image sharpness assessment in autoregressive parameter space," *IEEE Trans. Image Process.*, vol. 24, no. 10, pp. 3218–3231, Oct. 2015.
- [40] L. Li, W. Lin, X. Wang, G. Yang, K. Bahrami, and A. C. Kot, "No-reference image blur assessment based on discrete orthogonal moments," *IEEE Trans. Cybern.*, vol. 46, no. 1, pp. 39–50, Jan. 2016.
- [41] K. Gu, J.-F. Qiao, and W. Lin, "Recurrent air quality predictor based on meteorology-and pollution-related factors," *IEEE Trans. Ind. Informat.*, 2018, doi: [10.1109/TII.2018.2793950](https://doi.org/10.1109/TII.2018.2793950).



**Ke Gu** received the B.S. and Ph.D. degrees in electronic engineering from Shanghai Jiao Tong University, Shanghai, China, in 2009 and 2015, respectively.

He is currently an Associate Professor with the Beijing University of Technology, Beijing, China. His research interests include image analysis, environmental perception, quality assessment, machine learning, and big data analysis.

Dr. Gu was the recipient of Best Paper Award at the IEEE International Conference on Multimedia and Expo in 2016, and the Excellent Ph.D. Thesis award from the Chinese Institute of Electronics in 2016. He was the Leading Special Session Organizer in VCIP2016 and ICIP2017, and serves as the Guest Editor in the Digital Signal Processing journal. He is currently an Associate Editor for IEEE ACCESS, and is the reviewer for 20 top SCI journals.



**Xiaoli Li** received the bachelor's and master's degrees in control theory and control engineering from Dalian University of Technology (DUT), Durban, South Africa, in 1994 and 1997, respectively, and the Ph.D. degree in control science and engineering from Northeastern University, Shenyang, China, in 2000.

He is currently a Professor with the Department of Control Science and Engineering, University of Science and Technology Beijing, Beijing, China.

In 2006, he was the recipient of "Nova of Science and Technology of Beijing Municipality" of China, and "New Century Excellent Talents" of Ministry of Education of the People's Republic of China. His research interests include multiple model control, adaptive control, and visual tracking.



**Jun-Fei Qiao** (M'11) received the B.E. and M.E. degrees in control engineering from Liaoning Technical University, Fuxin, China, in 1992 and 1995, respectively, and the Ph.D. degree in control science and engineering from Northeast University, Shenyang, China, in 1998.

From 1998 to 2000, he was a Postdoctoral Fellow with the School of Automatics, Tianjin University, Tianjin, China. He joined the Beijing University of Technology, Beijing, China, in 2001, where he is currently a Professor. He is the Director of the Intelligence Systems Laboratory.

His current research interests include neural networks, intelligent systems, self-adaptive/learning systems, and process control systems.

Dr. Qiao is a member of the IEEE Computational Intelligence Society. He is a Reviewer for more than 20 international journals, such as the IEEE TRANSACTIONS ON FUZZY SYSTEMS and IEEE TRANSACTIONS ON NEURAL NETWORKS AND LEARNING SYSTEMS.